Materials Horizons

ROYAL SOCIETY OF CHEMISTRY

COMMUNICATION

View Article Online
View Journal | View Issue

Check for updates

Cite this: *Mater. Horiz.*, 2025, **12**, 8153

Received 22nd May 2025,
Accepted 30th June 2025

DOI: 10.1039/d5mh00971e

rsc.li/materials-horizons

Ferroelectric nematic and smectic liquid crystals with sub-molecular spatial correlations†

Parikshit Guragain, ‡[a] Arjun Ghimire,‡[b] Manisha Badu,[b] Netra Prasad Dhakal,[c] Pawan Nepal,[a] James T. Gleeson, [b] Samuel Sprunt, *[bc] Robert J. Twieg*[a] and Antal Jákli *[bc]

Nematic liquid crystals are anisotropic fluids which have long-range one-dimensional orientational order and short-range spatial correlations corresponding to the molecular length *L*. In X-ray studies this is manifested as diffuse peaks along the average direction of the molecular long axis at $Q = 2\pi/L$ and weaker harmonics at $2Q$ and $3Q$ wave numbers. This is the case for the recently discovered ferroelectric nematic (N_F) liquid crystals as well. Here we synthesized highly polar three ring rod-shaped compounds with a terminal thiophene ring which on cooling from the isotropic fluid directly transition to the N_F phase that shows the strongest spatial correlations corresponding to 1/3 of the molecular length ($L/3$). The set of thiophene compounds reported here have ferroelectric polarizations about 20% larger than that of usual ferroelectric nematic liquid crystal materials. This is the result of the tighter molecular packing and larger mass density, due to the lack of flexible terminal chains of these thiophene compounds compared to most of the N_F materials. Below the N_F phase, compounds with a single nitro or two cyano polar groups on the terminal benzene ring exhibit a so far never observed smectic phase with periodicity ~1/3 the molecular length. Based on our experimental results, we propose a model of this phase featuring antipolar packing of the molecules within the layers.

New concepts

Nematic liquid crystals are anisotropic fluids which have long-range one-dimensional orientational order and short-range spatial correlations corresponding to the molecular length, *L*. In X-ray studies this is manifested as diffuse peaks along the average direction of the molecular long axis (director) at $Q = 2\pi/L$ and weaker harmonics at $2Q$ and $3Q$ wave numbers. This is the case for the recently discovered ferroelectric nematic (N_F) liquid crystal phase as well. Here we report a new class ferroelectric nematic phase forming mesogens with stiff, strongly dipolar molecules lacking any terminal or lateral aliphatic substituents. In contrast to all N_F materials with flexible terminal chains, in the reported thiophene compounds the strongest spatial correlations correspond to one third of the molecular length instead of the full molecular length. All the studied thiophenes transition directly from the isotropic to N_F phase where they have ferroelectric polarizations of $P_S \approx 8\ \mu C\ cm^{-2}$, which is about 20% larger than of other N_F materials. This is due to their about 20% greater mass density compared to most of the N_F materials with short terminal chains. Furthermore, the thiophene compounds with a nitro group or two cyano polar groups on the C ring, exhibit a more ordered smectic phase, which is quite unusual behavior for molecules having no clear distinction between aromatic and aliphatic parts. Finally, we propose a tentative molecular packing model that explains both the unique spatial correlations of these compounds both in the ferroelectric nematic and the smectic phase.

1. Introduction

The long-sought ferroelectric nematic N_F liquid crystal phase, wherein macroscopic polar order is combined with 3-dimensional fluidity, was recognized[1] after several groups independently synthesized materials 3(4) CN,[2] DIO[3] and **RM734**[4] consisting of rod like molecules having permanent dipole moments of 10 Debye or greater. In the N_F phase, these electric dipoles spontaneously align in a common direction. This results in a macroscopic polarization

$$\vec{P}_S = \frac{\langle\vec{\mu}\rangle \rho N_A}{M} = \frac{S_P \vec{\mu} \rho N_A}{M}, \quad (1)$$

where ρ is the mass density, $N_A \approx 6 \times 10^{23}$ is Avogadro's number, M is the molar mass, $\langle\vec{\mu}\rangle = S_P\vec{\mu}$ is the spatial average molecular dipole moment, where $\vec{\mu}$ is the individual molecular dipole moment and $S_P \leq 1$ is the dipolar order parameter. Assuming typical values such as $\mu = |\vec{\mu}| \approx 10$ D (3.3×10^{-29} C m^{-1}), $\rho \approx 1.3 \times 10^3$ kg m^{-3},[5] $M \approx 0.4$ kg, we obtain $P = 6.4 \times 10^{-2}$ C m^{-2} for perfect polar order ($S_P = 1$). Experimental

[a] *Department of Chemistry and Biochemistry, Kent State University, Kent, OH 44242, USA. E-mail: rtwieg@kent.edu*
[b] *Department of Physics, Kent State University, Kent, OH 44242, USA. E-mail: ssprunt@kent.edu*
[c] *Materials Science Graduate Program and Advanced Materials and Liquid Crystal Institute, Kent State University, Kent, OH 44242, USA. E-mail: ajakli@kent.edu*

† Electronic supplementary information (ESI) available. See DOI: https://doi.org/10.1039/d5mh00971e

‡ These authors contributed equally to this work.

observations on N_F material[3,6,7] are consistent with $S_P \geq 0.95$. This spontaneous polarization is significantly larger than is typically observed in chiral SmC* smectic ferroelectrics[8–10] and polar bent-shape smectic liquid crystals.[11] Since their discovery, N_F materials have attracted significant interest because of their extraordinary physical properties such as large ferroelectric polarization, ultra-low ($E \leq 1$ V mm^{-1}) threshold field, sub millisecond switching time, large apparent dielectric constant, strong electrowetting, electromechanical instability, thermomechanical coupling, filament formation.[12–25] Since polar materials also lack inversion symmetry, N_F materials also show remarkable linear electromechanical responses,[26] large second harmonic generation (SHG)[22,27,28] due to large second-order non-linear optical (NLO) coefficients,[29,30] exotic entangled photon-pair generation,[31] and bulk photovoltaic effect[32] that hold promise for new technological applications.

Since 2017, hundreds of individual compounds exhibiting the N_F phase have been reported, but most belong to a few discrete structural classes.[33–42] As work proceeds to explore the physical properties of existing materials, researchers are also striving to define structure–function relationships that would guide the synthesis of next-generation materials. The creation of diverse sets of N_F materials is a prerequisite both to thoroughly understanding the physics of this novel phase and achieving real-world applications. Furthermore, the understanding of what governs not only the macroscopic properties but also the microscopic structure of these fluid polar materials remain at an early stage. One can anticipate that, in addition to entropic considerations and the ease at which fluids can reorganize themselves, electrostatic molecular interactions will be of primary importance. From this it necesserily follows that intermolecular distances will also be a dominating factor.

In this work, we report the synthesis, phase behavior, and critical physical properties – polarization value, mass density, and nanostructural organization – of a series of novel thiophene based three ring ferronematic compounds. Polarized optical microscopy (POM), X-ray scattering, ferroelectric polarization and mass density measurements are used to demonstrate the existence of the N_F phase and characterize its nanostructure. The materials exhibit larger ferroelectric polarization and mass density than previously reported in the N_F phase. In some cases, evidence for a lower temperature smectic phase with a unique 1/3 molecular length layering is observed. Tentative models to explain the 1/3 molecular length spatial correlations in the N_F phase and layering in the smectic phase are also described.

2. Results

2.1. Materials

Previously the N_F phase has been reported in compounds like DIO,[3] LC1 and LC2[43] which have saturated heterocyclic rings. The new compounds we prepared are of heteroaromatic ring-based N_F compounds that incorporate a thiophene ring. The thiophene ring has already been widely utilized in liquid crystal research to obtain conventional nematic,[44] smectic, columnar,

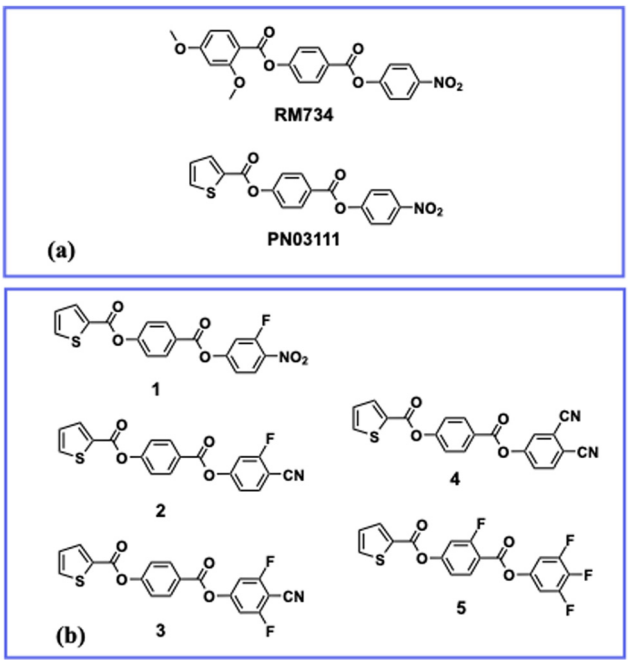

Fig. 1 Molecular structures of the materials relevant to this work. (a) The reference substances: 4-[(4-nitrophenoxy)carbonyl]phenyl 2,4-dimethoxybenzoate (**RM734**) (top) and 4-[(4-nitrophenoxy)carbonyl]phenyl-2-thiophenecarboxylate **PN03111** (bottom). (b) Structures of the five thiophene materials described in detail in this study.

and blue phases[45–48] and recently ferroelectric nematic phases.[49] Here, the important structure modification implemented is the substitution of a thiophene group as the A-ring in lieu of a benzene A-ring found in the prototypical N_F **RM734**.[4] The thiophene ring emulates the 2,4-dimethoxybenzene electronically and spatially without any need for additional substituents. Equally important, and in further contrast to most previously reported N_F materials, these compounds have no flexible ''tail'' groups such as the two methoxy substituents in **RM734**.

Fig. 1 displays the molecular structures of the thiophene compounds studied, together with two reference materials: a prototypical N_F (**RM734**) and the parent thiophene analog of **RM734** (**PN03111**).[42] **RM734** features an all-benzene core with internal linking groups (two esters) and terminal functional groups (ethers and nitro) arranged such that their bond and group dipoles align, resulting in a large net molecular dipole. Typical **RM734**-like N_F compounds are characterized by short terminal substituents along the director axis and an unusual *ortho* substituent on the terminal A-ring. In **PN03111**, the A-ring of **RM734** is replaced by a 2-thiophene ring with no additional substituents.

The five primary materials investigated in this paper (Fig. 1(b)) share the same core framework as **PN03111**, differing only in the substituents positioned on the B and C rings. In contrast to the I–N transition of **RM734**, these compounds as well as **PN03111** have a direct I–N_F transition on cooling. Compared to **PN03111**, compound **1** features an additional fluorine substituent *ortho* to the terminal nitro group. This

modification lowers the clearing point (transition to isotropic phase) by about 30 °C, avoiding the risk of thermal decomposition over time at elevated temperature, which occurs with **PN03111** and which makes its physical property characterization less reliable. Both compound **1** and **PN03111** exhibit a positionally ordered (smectic) phase when cooled below the N_F phase.

Compound **2**, structurally resembles compound **1**, but features a less polar cyano group in place of the terminal nitro group. This substitution significantly reduces the molecular dipole moment. Despite this change, the N_F remains present in compound **2**. Interestingly, the N_F phase range broadens in compound **2**, and the isotropic temperature is further reduced, relative to compound **1**.

Compound **3** adds a second fluorine in the *ortho* position compared to compound **1**. This modification increases the N_F-isotropic transition temperature, while also broadening the N_F phase range. The 130 °C wide N_F temperature range of this compound is noteworthy and highlights the significant impact that an extra polar bond near the terminal groups can have on the N_F behavior of these materials.

Compound **4** contains two adjacent cyano groups at the *meta* and *para* sites of the C ring. Compared to the structurally similar compound **2**, it exhibits a slightly lower N_F-isotropic tranistion temperature. The presence of the large and rigid *meta* cyano group in **4** contributes to in a less stable N_F phase, characterized by a reduced phase range, compared to the systems with a fluorine atom at this site. Additionally, a smectic phase appears in this compound below the N_F phase.

Compound **5** features a distinct substitution pattern, lacking any large polar group at the terminal position. Instead, it has three highly electronegative fluorine atoms at the *para* and two *meta* positions on the C ring and an additional fluorine atom substituent on the B ring, which is unique amongst the materials studied here. The B-ring substitution is crucial, as the analogous compound (not further discussed here) without this additional fluorine atom exhibits a metastable N_F phase with a range of only 1 °C.

The molecular structures, phase sequences and dipole moments of the materials studied are listed in Table 1. The isotropic phase above the N_F phase is denoted by I, and the mesophases observed below the N_F phase for **1**, **4** and **PN03111** above the crystal phase are labeled by X.

2.2. Polarizing optical microscopy

Representative polarizing optical microscopy (POM) images of 5 μm thick films of compounds **1–5** contained between planar substrates treated with anti-parallel rubbed polyimide alignment layers are shown in Fig. 2.

On cooling from the isotropic phase, the N_F phase appears *via* nucleation of circular shaped domains as recently described for other materials having direct I–N_F transitions.[27,50] In this I/N_F coexistence range, for compounds **1** and **3**, the texture of the N_F domains with circular cross-sections has dark brushes that meet at the domain center: the brushes are along crossed polarizer and analyzer directions. This texture corresponds to tangential polarization direction with a circular line defect at the center.[50] In compounds **4** and **5**, the horizontal brushes are replaced by green brushes in a pink background. Such textures may be indicative of a biaxial director structure, whose origin is beyond the scope of this paper. The texture of the N_F droplets coexisting in the isotropic phase of compound **2** is even more complicated.

Table 1 List of structural features, the phase sequence, dipole moments calculated using Chem3D Ultra MOPAC, and the molecular lengths calculated by ChemOffice of the studied thiophene compounds

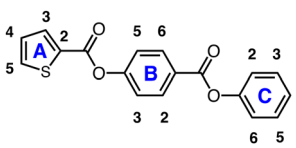

	Structure (substituent sites numbered)			Physical properties		
#	Ring A	Ring B	Ring C	Dipole moment (D)	Molecular length (nm)	Phase sequence (°C)
1	2-Thiophene	—	3-F, 4-NO_2	11.19	1.83	Cr 189 **N_F** 207 I 204 **N_F** 162 × 130 Cr
2	2-Thiophene	—	3-F, 4-CN	8.71	1.83	Cr 167 **N_F** 192 I 191 **N_F** 101 Cr
3	2-Thiophene	—	3,5-F, 4-CN	9.74	1.86	Cr 162 **N_F** 211 I 209 **N_F** 105 Cr
4	2-Thiophene	—	3,4-CN	9.97	1.86	Cr 182 **N_F** 184 I 182 **N_F** 149 × 80 Cr
5	2-Thiophene	2-F	3,4,5-F	8.81	1.75	Cr 139 **N_F** 153 I 152 **N_F** 123 Cr
PN03111	2-Thiophene	—	4-NO_2	10.28	1.81	Cr 234 I 215 **N_F** 176 × 152 Cr
RM734	2,4-Dimethoxy benzene	—	4-NO_2	11.40	2.05	Cr 140 N 190 I 189 N 133 **N_F** 75 Cr

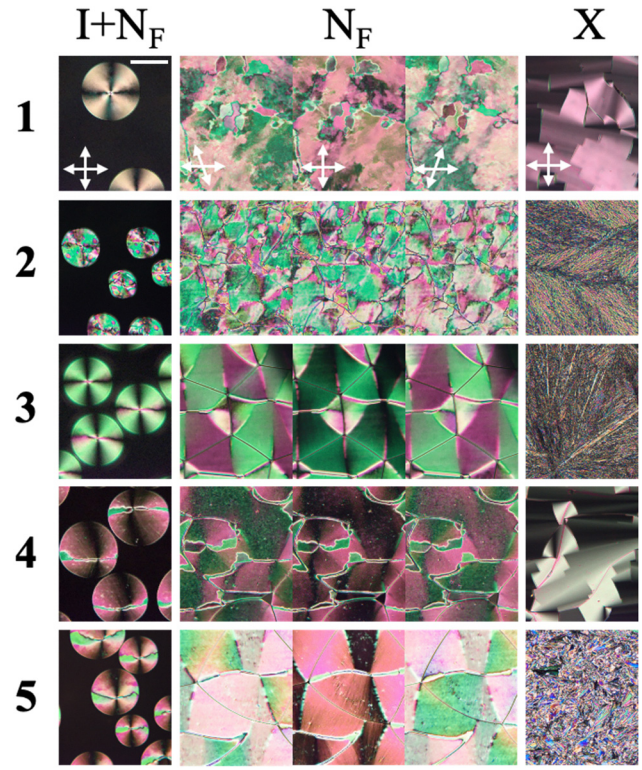

Fig. 2 Representative polarizing optical microscopy (POM) images of compounds **1–5** in the I/N$_F$ coexisting range, in the N$_F$ phase, and in the respective lower temperature phase forming below the N$_F$ phase. The length of scalebar on image **1** is 50 μm.

The textures in the fully formed N$_F$ phase are characterized by various marble or mosaic-type patterns in which the initial N$_F$ domains are separated by straight (compound **3**) or arc shaped (compound **5**) defect lines, while for **1**, **2** and **4** the defect lines are irregular. Looking at the N$_F$ textures between oppositely uncrossed polarizers, we note that the same birefringence colors of certain domains split into different colors that exchange under opposite uncrossing directions. This can be best seen in compound **3**, where the original dark green domains split into magenta and light green areas. These observations indicate oppositely twisted domains along the film thickness, as expected for N$_F$ materials sandwiched between substrates with anti-parallel alignment layers. Below the N$_F$ phase the textures indicate crystal phases for compounds **2**, **3** and **5**, and either columnar or smectic phases for compound **1** and **4**, respectively. Looking at Table 1, we can see that these two compounds (**1** and **4**) have the largest dipole moments, which may be related to the formation of the higher ordered LC phase(s).

2.3. X-ray diffraction

Small-angle X-ray scattering (SAXS) results on our thiophene compounds **1–5** and (for comparison) **RM734** are summarized in Fig. 3–5. Fig. 3 shows two-dimensional SAXS patterns recorded at representative temperatures in the N$_F$ phase of compounds **1–5** and (for comparison) **RM734**, as well as in the X phase observed in compounds **1** and **4** only. In the N$_F$ phase (top two rows of Fig. 3), all compounds produce three diffuse arcs of scattering along the magnetically-aligned director, indicating short-range positional correlations at roughly one, one half, and one third the molecular length (scattering wavenumbers Q_1, Q_2 and Q_3, respectively). However, particularly in compound **4**, the diffraction at the lowest angle (Q_1) appears to be split into two lobes along the azimuthal direction. Along the axis orthogonal to the director and at wider angle are diffuse peaks associated with short-range, liquid-like lateral correlations between the molecules. For similar scaling of the intensity levels relative to the maximum intensity in the images, the thiophene compounds generally produce stronger small angle diffraction along the director axis than **RM734** in the N$_F$ phase, particularly in the peak at Q_3 corresponding to the positional correlations at $\sim$1/3 the molecular length.

In the X phase of compounds **1** and **4** (bottom row of Fig. 3), the width of this peak narrows considerably, and its intensity saturates in the images at bottom left and center in Fig. 3. This signifies the development of one-dimensional long-range positional order (smectic phase), which, particularly in compound **4**, is accompanied by a rotation of the axis of the diffuse wide angle diffraction off its original direction in the N$_F$ phase. After rescaling the intensity levels in the image at the bottom right in Fig. 3, we see that the wide angle rotation is associated with an azimuthal splitting of the smaller angle Q_3 peak, which indicates the presence of differently oriented domains in the smectic phase. Here we note that the appearance of a smectic phase in liquid crystals without long flexible terminal chains is very unusual, as a smectic phase typically requires nanophase separation between rigid-cores and flexible tails.

Fig. 4 plots the wavenumber (Q) dependences of the scattering intensity averaged azimuthally over the angular range indicated by the blue annulus outlines in Fig. 3. Results are shown for **RM734** and for compounds **1–5** at four different relative temperatures ($\Delta T = T - T_{I\text{–}N_F}$) below the isotropic to N$_F$ phase transition.

The positions of the three small angle peaks (wavenumbers Q_1, Q_2 and Q_3) show no temperature dependence in the N$_F$ phase. For compounds **1–4** they are $Q_1 \approx 3.2$ nm^{-1}, $Q_2 \approx 2Q_1 \approx 6.6$ nm^{-1} and $Q_3 \approx 3Q_1 \approx 10.0$ nm^{-1}, with Q_1 corresponding to a length $L = 2\pi/Q_1 \approx 1.95$ nm, while for compound **5** they are slightly larger, $Q_1 \approx 3.5$ nm^{-1}, $Q_2 \approx 2Q_1 \approx 7.0$ nm^{-1} and $Q_3 \approx 3Q_1 \approx 10.7$ nm^{-1}, corresponding to $L \approx 1.8$ nm. These lengths are slightly ($\sim$3%) larger than the the stretched molecular lengths L_S calculated by ChemOffice and shown in Table 1.

Strikingly, while for **RM734** and other materials with an N$_F$ phase[42,51–54] the scattering intensity (I) of the small angle peaks decreases monotonically at larger Q values, for the thiophene compounds **1–5** the peak at Q_3 is stronger than at Q_1 and Q_2. In fact, except for compound **5**, $I_{Q_3} > I_{Q_2} > I_{Q_1}$. In the higher order LC phase (X phase) observed in compounds **1** and **4**, the width of Q_3 peak is less than our resolution limit ($\sim$0.18 nm^{-1}). At the transition to the X phase, Q_1 and Q_2 increase by $\Delta Q_1 \approx \Delta Q_2 \approx 0.2$ nm^{-1}, while Q_3 is unchanged. As pointed out in

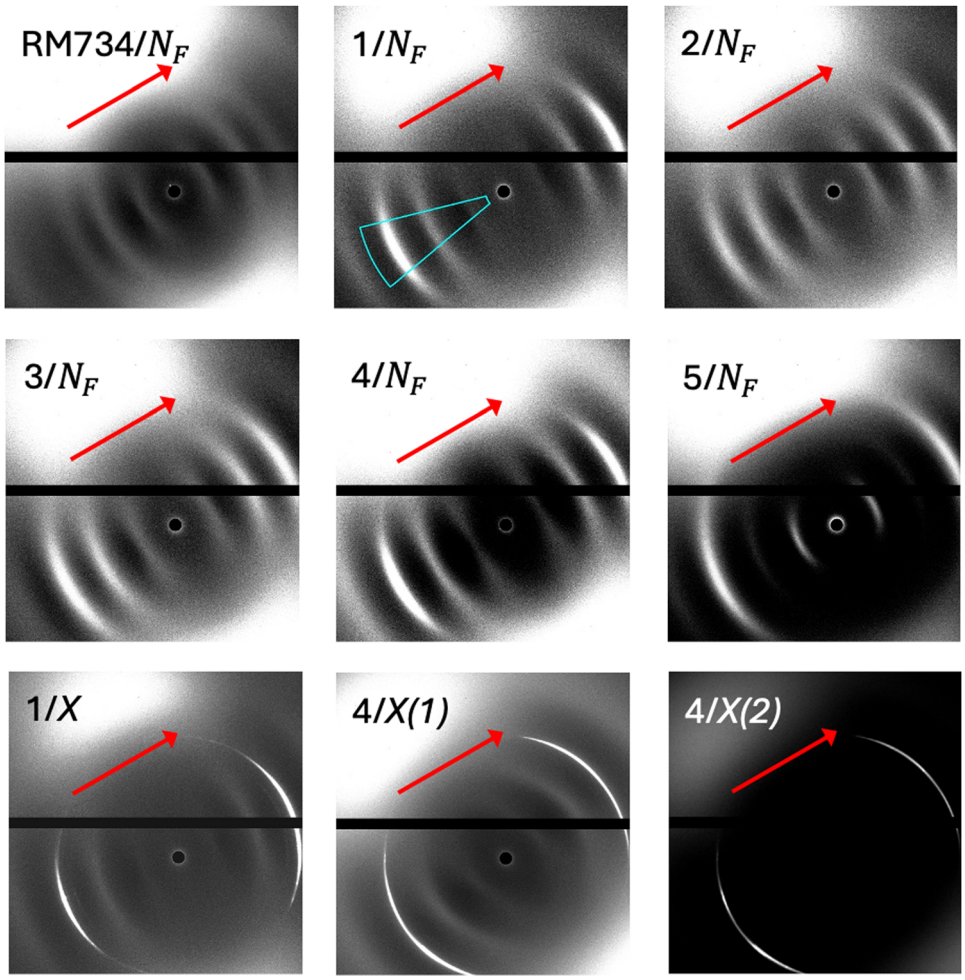

Fig. 3 Two dimensional SAXS patterns recorded on thiophene compounds **1–5** and (for comparison) on **RM734** at representative temperatures in the middle of the N_F phase (top two rows). In the bottom row also shown are SAXS patterns in the X phase, recorded at temperatures just below the N_F–X transition in compounds **1** and **4**. The red arrows indicate the direction of a magnetic field applied to align the nematic director. The blue outline shows the section of the annulus in which angular averages were taken to produce the radial profiles (Q dependence) of the scattered X-ray intensity in Fig. 4.

connection to the bottom pictures of Fig. 3, the X-ray patterns in the X phase in compounds **1** and **4** mainly differ from the N_F phase by the intensity and sharpness of the Q_3 peak. In compound **1** the peak remains centered on the axis of the aligning magnetic field, which would indicate an orthogonal smectic A phase. As pointed out above, an apparent rotation of the diffraction pattern in the X phase of compound **4** is actually the result of a breakup into domains with different orientations of a smectic A type layer structure.

The position of our XRD detector was optimized to record the small angle scattering associated with positional correlations along the average long axis of the molecules, and the diffuse high angle scattering along the lateral directions is only partially recorded within the angular range subtended at the detector position. Nevertheless, azimuthal averages over the limited range available yield a single, broad peak centered at $q \sim 14$ nm^{-1} with FWHM ~ 6 nm^{-1} for all the thiophene materials studied. Assuming hexagonal local lateral packing and using $a = \frac{4\pi}{Q \cdot \sqrt{3}}$ for the side length of the hexagon, we estimate the average lateral distance between the molecules to be $a \approx 5.1$ Å. This is smaller than the $a \approx 5.6$ Å reported for **RM734** by Mertelj *et al.*[54] This clearly indicates that the lateral packing of the thiophene molecules without flexible tail are tighter than of **RM734** with two methoxy substituents. There is no evident splitting that would proof biaxial packing, although the peak is too broad to rule out the possibility.

We calculate correlation length, ξ, as 2π divided by full width at half maximum of the peak. The temperature dependences (relative to the N_F-Iso transition temperature) of all three correlation lengths are shown in Fig. 5. In the case of **RM734**, on cooling, the correlation length associated with the peak at Q_1 increases from 2 nm to 6 nm, *i.e.*, from about 1 to 3 molecular lengths, while the correlation length associated with the peaks at Q_2 and Q_3 remain constant at ~ 4 nm and decrease from ~ 4 nm to ~ 2 nm, respectively. These values are typical for nematic materials with very short spatial correlations.[55] In contrast to **RM734** and similar N_F compounds, the correlation length for short range ordering in the thiophene compounds **1–5** is the greatest at the length scale $L/3$ (*i.e.*, the width

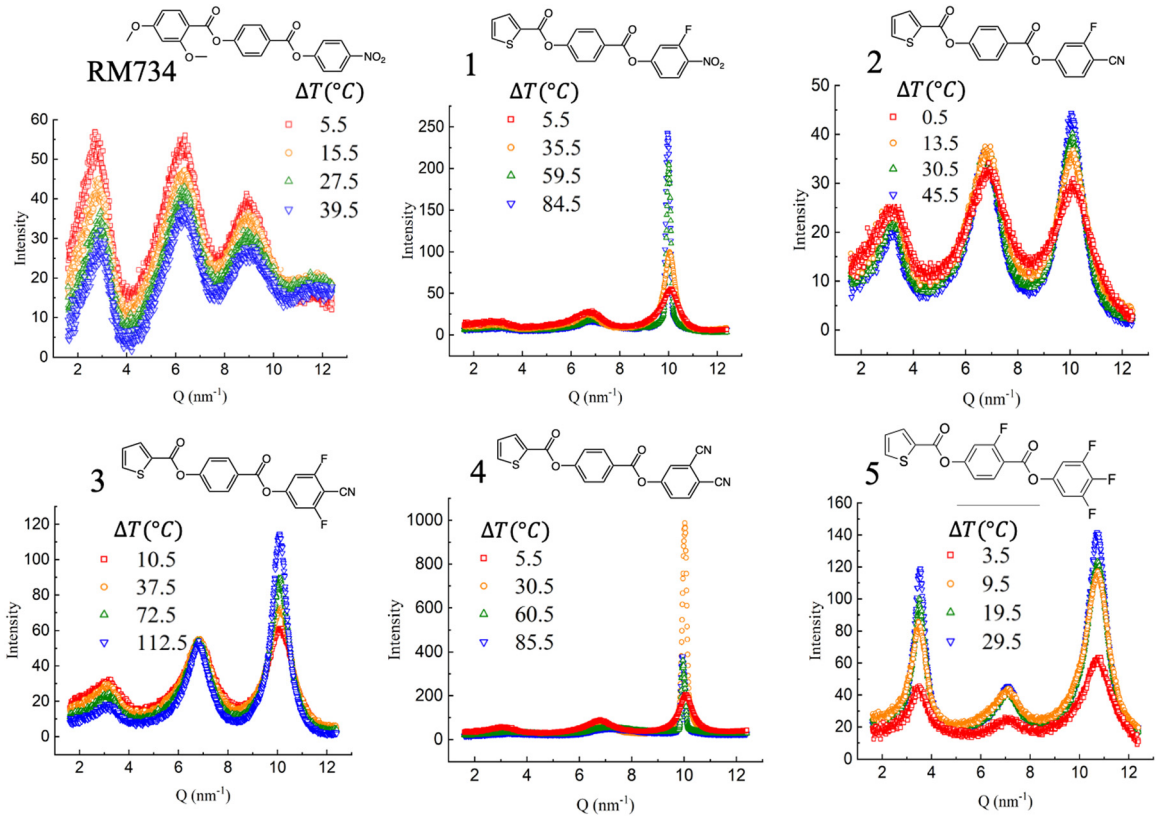

Fig. 4 Molecular structures and wavenumber (Q) dependences of the scattering intensities in 1.5–12 nm^{-1} range for **RM734** and for compounds **1–5** at 4 different relative temperatures ($\Delta T = T - T_{I-N_F}$) below the isotropic – N_F phase transition.

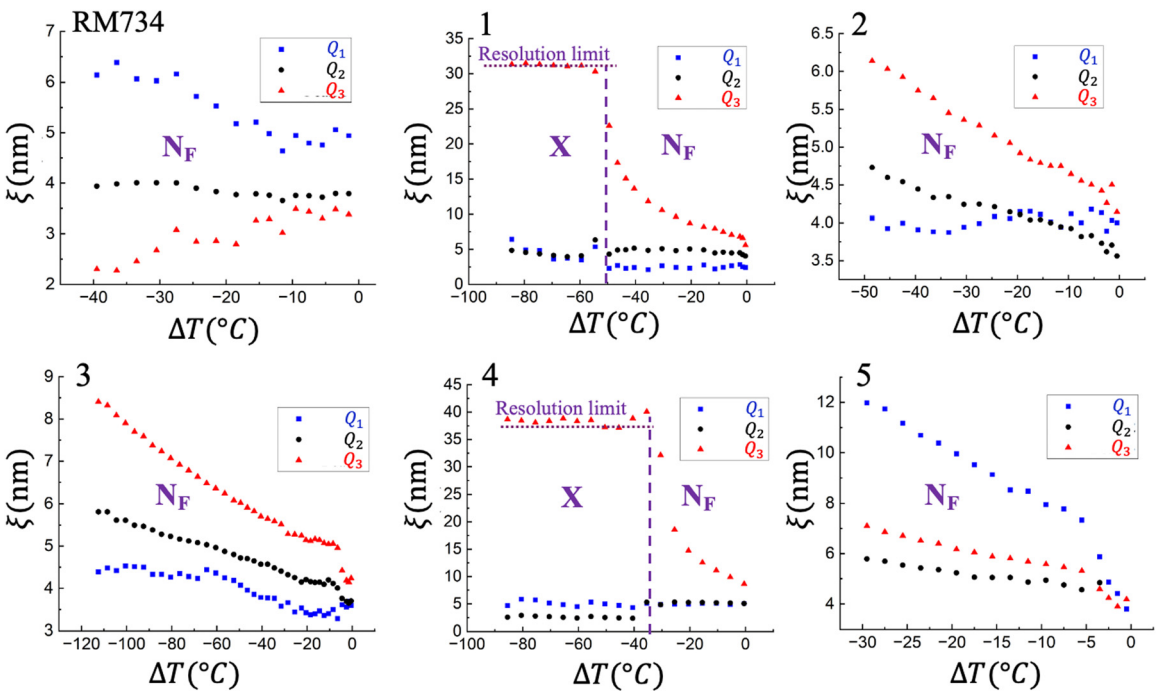

Fig. 5 Relative temperature ($\Delta T = T - T_{I-N_F}$) dependences of the correlation lengths $\xi = 2\pi/FWHM$, where FWHM stands for full width at half maximum of the peak, for **RM734** and for the compounds **1–5**.

of the peak at Q_3 is the narrowest). Except for compound **5**, the correlations associated with ordering at L have the shortest range (of the three), the opposite of what we observe in **RM734**, and what has been reported for another prototypical N_F, the compound DIO.[24] Compounds **2**, **3** and **5**, *i.e.*, those that have a crystal phase below the N_F, have relatively short (between 2 nm and 12 nm) correlation lengths; these typically increase as the temperature is decreased. In compounds **1** and **4**, the correlation length associated with the peak at Q_3 shows a strong increase in the N_F phase on cooling, reaching ~30 nm before transitioning to the highly ordered LC phase where the peak width reaches our experimental ability to measure, *i.e.* resolution limit, $\Delta Q \approx 0.18\ \mathrm{nm}^{-1}$. On the other hand, the correlation lengths associated with the peaks at Q_1 and Q_2 are in the 2–8 nm range and are almost temperature independent.

2.4. Polarization and density measurements

Fig. 6(a) shows the relative temperature ($T - T_{I\text{–}N_F}$) dependences of the ferroelectric polarizations of compounds **1–5** determined from the area of the current peak above the baseline determined by the ohmic current measured under 50 Hz triangular voltages. It is found that P_S is independent of the frequency in the range 40 Hz $\leq f \leq$ 100 Hz. A representative time dependence of the current flowing throught the sample is shown in the lower inset for compound **4** at 176 °C under 50 Hz 30 V amplitude triangular voltage. It can be seen that the current peak due to polarization switching is dominating over the resistive and capacitive currents. For all compounds P_S increases sharply below the I–N_F transition reaching about 90% of the highest value within 3 °C below $T_{I\text{–}N_F}$. Further away from $T_{I\text{–}N_F}$, P_S increases only slightly, reaching $P_S \approx 7.6\text{–}8\ \mu\mathrm{C\ cm}^{-2}$ by $T - T_{I\text{–}N_F} \approx -15$ °C. We note that, although the smectic phase of compounds **1** and **4** looks similar to the SmA_F of several highly polar materials below the N_F phase,[52,56–58] we could not measure ferroelectric polarization up to 500 V (more than 10 times higher than needed in the N_F phase) applied between 5 mm in-plane gap. This is either because switching the polarization in the polar smectic phase requires higher fields, or because the smectic phase is not polar.

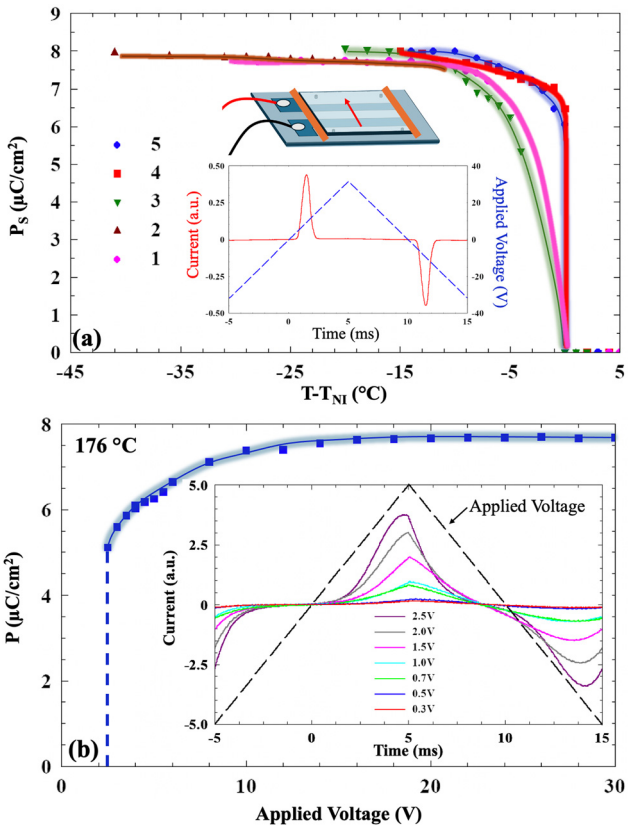

Fig. 6 Summary of the polarization measurements of the studied thiophene compounds. (a) Main pane: Relative temperature dependences of the measured polarizations of compounds **1–5** obtained at f = 50 Hz calculated from the area of the current peak above the baseline determined by the ohmic current as shown for compound **4** at 176 °C in the lower inset. Upper inset illustrates the geometry of the cells used for the measurements. (b) Main pane: Voltage dependence of the polarization of compound **4** at 176 °C. The inset shows the time dependence of the polarization current at different applied voltages.

The upper inset shows the sketch of the in-plane cell used for the polarization measurements. The red arrow shows the rubbing direction of the PI deposited on the bottom plate and of the direction in which the compound is filled into the cell.

Fig. 6(b) shows the voltage dependence of the apparent polarization for compound **4** at 176 °C. As can be seen in the inset of Fig. 6(b), the polarization peak becomes symmetric similar to the situation shown in the inset to Fig. 6(a) above 2.5 V. Below that the time dependent current is asymmetric: there is an increase of the slope under $V > 0$ V when the voltage increases from $V < 0$ V, whereas the current slope is constant under decreasing voltages, but reaching minimum above the lowest voltage value. This asymmetric behavior might indicate some polar arrangement below 2.5 V. This is likely related to a small pretilt α of the director, yielding a small vertical component of the polarization $P = P_S \sin\alpha$, and consequently a depolarization field $E_{dep} = -\dfrac{P_S \sin\alpha}{\varepsilon_0 \varepsilon}$.

It is significant that the measured saturated polarization values P_S are consistently larger than $P_S \approx 6.4\ \mu\mathrm{C\ cm}^{-2}$ that has been both reported[1] and confirmed by us for **RM734**, which actually has a greater dipole moment than any of compounds **1–5**. To resolve this apparent contradiction, we look to eqn (1). With similar polar order parameter and molecular mass, a greater polarization with lesser dipole moment is only possible with correspondingly greater mass density. Numerical estimates for **RM734**,[1] and precision density measurements on another room temperature N_F mixture[5] give their densities $\varrho \approx 1.3\ \mathrm{kg\ m}^{-3}$; values that are already 30% larger than for typical nematic liquid crystals.

Without having sufficient quantities of our compounds for commercial density instruments,[5] we conducted a preliminary density determination by measuring column length of a known mass of material confined without air bubble in a uniform cylindrical capillary. These measurements give $\varrho_{1\text{–}5} \approx 1.54 \pm 0.03\ \mathrm{kg\ m}^{-3}$ for compounds **1–5**, and $\varrho_{RM734} \approx 1.3 \pm 0.03\ \mathrm{kg\ m}^{-3}$ for **RM734**. Thus, the compounds reported

here, even with lower dipole moment have sufficiently greater density to explain their larger polarization. This increased density agrees with the smaller lateral distances between molecules indicated by non-optimised wide angle scattering results. The implications of this are discussed below.

3. Discussion

We synthesized and studied the physical properties of highly polar rod-shaped compounds where a thiophene ring replaced the 2,4-dimethoxybenzene ring of **RM734**. This change made the following notable changes compared to **RM734** and most other N_F materials in this class. (i) On cooling there is no paraelectric nematic phase below the isotropic phase; instead, the studied thiophenes transition directly from the isotropic to N_F phase. (ii) In contrast to all N_F materials with flexible terminal chains with relatively large separation between neighboring molecules, in thiophene compounds there are strong spatial correlations corresponding to one third of the molecular length instead of the weak spatial correlations with periodicity corresponding to the full molecular length. (iii) The thiophene compounds with a nitro group or two cyano polar groups on the C ring have a smectic phase instead of the usual crystal structure below the N_F phase. (iv) All studied thio phene compounds have ferroelectric polarizations of $P_S \approx 7.8 \pm 0.3$ μC cm^{-2}, which is about 20% larger than of **RM734**. (v) These compounds have about 20% greater mass density compared to **RM734** and most of the N_F materials with short terminal chains.

We propose that all these features can be attributed to a denser packing of our thiophene compounds **1–5** compared to other N_F materials having short terminal chains. When molecules are more closely packed, the interaction distance decreases which correspondingly increases the electrostatic forces that prefer the permanent dipoles to be oriented either oppositely in the same plane, or in a common direction when not positioned in the same plane. This has been discussed in various phases,[59–61] including recently by Madhusudana and for the N_F phase.[62,63] In Madhusudana's model, the N_F molecules are assumed to (a) freely rotate about their axes, and (b) have non-uniform electric charge density along their axis due to the dipolar groups attached to the highly polarizable phenyl rings. In this scenario, the electrostatic interaction energy between laterally adjacent molecules is most favorable when lower electron densities (a net positive charge) and higher electron densities (a net negative charge) are nearest.

Our thiophene molecules have three major dipoles: the first one corresponds to a dipole (NO_2, CN or F) attached to the C-ring; the second one is an ester group connected to the B ring; and the third one is another ester group connected to the thiophene ring. We used the molecular structure of **1** to sketch the possible molecular packing in the N_F phase and in the underlying smectic phase (see Fig. 7(a) and (b), respectively). The arrangement corresponding to the lowest electrostatic energy would result in a crystal structure and is not nematic. However, in the N_F temperature range, the thermal motion tends to randomize the positive–negative arrangement, yet still provide ferroelectric packing as we illustrate in Fig. 7(a). Whenever the positive–negative arrangement shift in the same direction for larger number of molecules, temporary skewed smectic-like correlations are realized with L periodicity. These are illustrated by dotted blue lines in Fig. 7(a). In layered smectic clusters the transverse component of the dipole moment prefers parallel arrangement, while the longitudinal component of the dipole moment prefers antiparallel orientation.[64] In our thiophene compounds the dipole moment is mainly longitudinal and the molecules pack closely. Therefore, we cannot exclude the possibility of the antiparallel dipole packing in the smectic clusters of the N_F phase. However, large

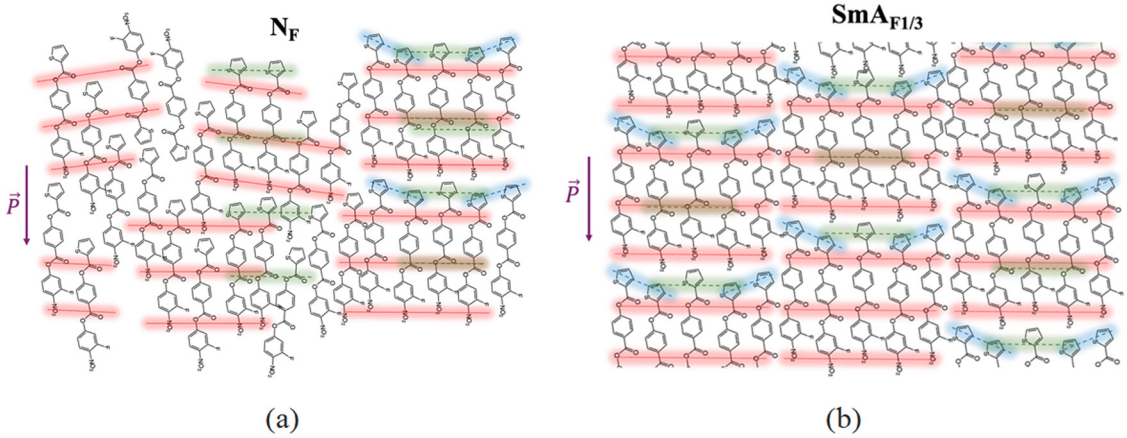

Fig. 7 Schematic illustration of the molecular packing in the N_F phase of compounds **1–5** (a) and in the smectic phase of compounds **1** and **4** (b) using the molecular structure of compound **1**. There are three aromatic rings C, B and A separated by $\sim L/3$ distances. The pink, green and light blue lines with glows indicate the $L/3$, $L/2$ and L length periodicities. In the majority N_F volumes of (a) we assume the molecules freely rotate about their long axes (uniaxiality), while in the cybotactic clusters we assume the planes of the aromatic rings tend to pack cofacial to each other although, in the sketch they shown in the same plane (non-cofacial) for simplicity.

volume of these clusters in the N_F phase would lead to decrease of the ferroelectric polarization, which is not compatible with the observed large polarizations with over 95% polar order (see Fig. 6(a)). The scattering intensity of the $L/3$ periodicity in the N_F phase is $\geq$10% of the peak in the smectic phase indicating the volume of the clusters with $L/3$ periodicity reaches at least 10% of the whole volume. This means the majority of them has ferroelectric packing as shown in Fig. 7(a). We note that the ferroelectric packing requires random up and down shift of the adjacent dipoles so that the negative charge of a dipole of one molecule will be next to the positive charge of the neighbor molecule in agreement with Madhusudana's model for the ferroelectric nematic phase.[62] This can lead to the SmA-type clusters as seen in Fig. 3 only if the up-and-down shifts are random, so the small angle X-ray diffraction would see the average direction perpendicular to the layer normal. The pink dotted lines with glows indicate these $L/3$ length periodicities. Clusters with potential $L/2$ periodicity are illustrated with green lines with glows. Additionally, we may assume the presence of clusters where the laterally neighbor molecules are shifted by half molecular length with alternating dipole directions to explain the $L/2$ periodicities. The fact that compound **5** with a fluorine atom in the central ring has a smaller peak with $L/2$ periodicity than with L periodicity, might indicate that the fluorine atom of ring B of one molecule is avoiding the sulphur atom in ring A of the neighbor molecules.

While in the majority N_F volumes we assume the molecules freely rotate about their long axes (uniaxiality), in the cybotactic clusters we assume the planes of the aromatic rings tend to pack parallel to each other (in contrast to the sketch in Fig. 7, where they are shown in the same plane for simplicity). Accordingly, the smectic clusters with $L/3$ and $L/2$ periodicities represent biaxial domains.

It is reasonable to assume that upon transition to the smectic phase in compounds **1** and **4**, the smectic clusters of the N_F phase coalesce and fill the entire volume as tentatively illustrated in Fig. 7(b). Although in the neighbor domains the aromatic rings pack together, they do so randomly, *i.e.*, the A ring can stick to the B or C, *etc.* Such arrangement will provide a long-range $L/3$ periodicity and only short-range order with L and $L/2$ periodictity. We note that parallel and antiparallel arrangements without or with $L/2$ longitudinal shifts could still be present as competing, short range structure giving rise to weak broad Q_1 and Q_2 signals. We have also neglected showing domains with slightly different orientations that we observed by X-ray diffraction (see bottom-right image of Fig. 3). To emphasize the 1/3 molecular length periodicity of this para-electric smectic phase, we denote it as $SmA_{1/3}$ phase. Although our tentative model assumes macroscopically polar packing such as the polar orthogonal smectic (SmA_F) phase observed previously for several other N_F materials,[52,56–58] due to the lack of polar switching, presently we do not have evidence for it.

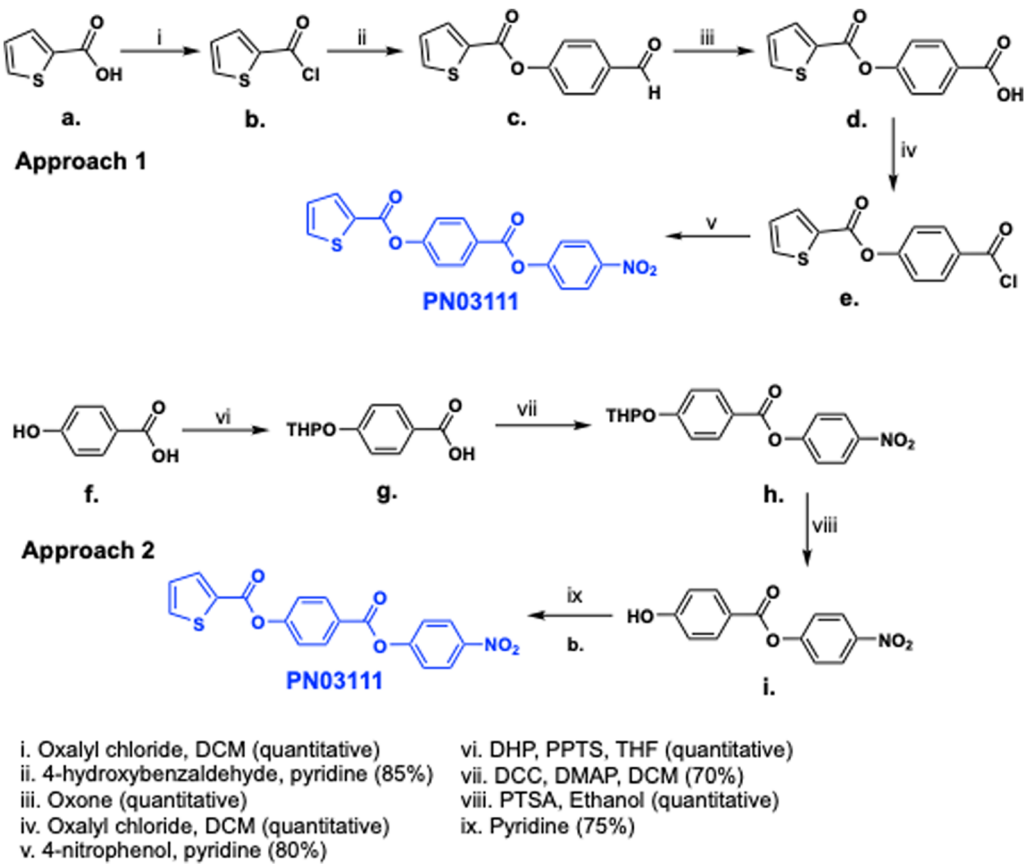

Fig. 8 Synthetic routes that are implemented for the synthesis of **PN03111** material.

Also, in the known SmA_F phases[52,56–58] the main periodicity is equal to the molecular length (L) in contrast to the $L/3$ periodicity of our $SmA_{1/3}$ smectic phase.

4. Methods

4.1. Chemical synthesis

The synthesis of these materials generally follows the methodology outlined in the scheme shown in Fig. 8. This scheme illustrates two distinct approaches employed to synthesize the reference compound **PN03111**.

In **Approach 1**, the synthesis begins with the assembly of the target molecule from the left side (A-ring), sequentially adding the central (B-ring) and right-side (C-ring) components. Conversely, **Approach 2** involves initial assembly of the central (B-ring) and right-side (C-ring), with the A-ring introduced in the final step. The primary synthetic methodology employed in both approaches is esterification. Notably, even when the acid chloride precursor is not commercially available and must be prepared, the acid chloride route is often preferred due to a significant reduction in the need for chromatographic purification during synthesis.

Approach 1 utilizes the commercially available precursor 2-thiophenecarboxylic acid (A-ring). This was first converted to its corresponding acid chloride **b** using oxalyl chloride. The acid chloride was then reacted with 4-hydroxybenzaldehyde in an esterification step to yield intermediate **c**. The aldehyde functional group of **c** was subsequently oxidized to a carboxylic acid using Oxone, producing the monoester carboxylic acid **d**. Intermediate **d** was converted to its acid chloride **e**, which was then subjected to a final esterification reaction with 4-nitrophenol to produce the target compound **PN03111**. This approach has high efficiency, with reaction yields ranging from 80% to higher, and provided clean products without requiring extensive purification steps.

Approach 2 starts with the commercially available precursor 4-hydroxybenzoic acid (**f**, B-ring). The phenolic functional group was initially protected with dihydropyran (DHP), yielding the THP-protected intermediate **g**. Esterification of **g** with 4-nitrophenol using the Steglich method followed by subsequent removal of the THP protecting group afforded the phenolic monoester intermediate **i**. Finally, after esterification reaction between **i** and 2-thiophenecarbonyl chloride **b** produced the target compound **PN03111**. Both approaches provide viable synthetic routes to **PN03111**, with the key distinctions lying in the order of ring assembly and the handling of intermediates. Synthesis details are provided in the ESI.†

4.2. Polarizing optical microscopy (POM)

For POM measurements an OLYMPUS BX60 microscope equipped with a Nikon D5600 camera was used. The LC samples were placed in heat stages controlled by METTLER FP90 temperature controller. 5 μm LC films were studied in cooling with 1 °C min^{-1} cooling rates.

4.3. X-ray measurements

Small angle X-ray scattering (SAXS) measurements were carried out in the Advanced Materials and Liquid Crystal Institute of Kent State University on a Xenocs Xeuss 3.0 SAXS/WAXS imaging beamline equipped with a Cu K_α source producing 8.05 keV X-rays (1.542 Å wavelength). The beam size at the sample was 0.9 mm, the sample-detector distance was 140 mm, and the detector's pixel size was 75 μm × 75 μm. The detector's active area (including detector gaps) was 77.1 mm × 79.65 mm. The resolution limit in scattering wavenumber Q of the recorded SAXS patterns is estimated to be $\Delta Q \sim 0.18$ nm^{-1}, which corresponds to 2/0.18–35 nm maximum detectable correlation length. The SAXS patterns were processed using Datasqueeze software to obtain the azimutally averaged scattered intensity, $I(Q)$. The latter was fit to the sum of three Pseudo-Voigt functions and a fixed background, which yielded values for the FWHM of the individual peaks at Q_1, Q_2, and Q_3 presented in Fig. 4.

4.4. Ferroelectric polarization measurements

The ferroelectric polarizations were measured using in-plane cells with d = 5 mm electrode gap as shown in the inset to Fig. 6(a). The electrode width and length are w = 2 mm and $l \approx 1$ cm respectively. The thickness of the cell is achieved by using $h = 10 \pm 0.2$ μm spacers. Triangular pulses of frequency f and peak-to-peak voltage of V were applied at various constant temperatures. The time dependence of the polarization current $I_P(t)$ is calculated by measuring the voltage drop (V_m) across a R = 20 kΩ resistor. After the polarization current drops back to the baseline with slope determined by the ohmic current I_Ω, the area above the ohmic baseline is calculated to give the spontaneous polarization value P_S as $P_S = \frac{\int V_m dt}{2R(l \cdot h)}$.

Conflicts of interest

There are no conflicts to declare.

Data availability

Data is available from the corresponding authors by reasonable requests.

Acknowledgements

This work was financially supported by US National Science Foundation grant DMR-2210083.

References

1 X. Chen, E. Korblova, D. Dong, X. Wei, R. Shao, L. Radzihovsky, M. A. Glaser, J. E. Maclennan, D. Bedrov, D. M. Walba and N. A. Clark, *Proc. Natl. Acad. Sci. U. S. A.*, 2020, **117**, 14021–14031.

2 D. Ziobro, J. Dziaduszek, M. Filipowicz, R. Dąbrowski, J. Czu and S. Urban, *Molecular Crystals and Liquid Crystals*, 2009, vol. 502, pp. 258–271.
3 H. Nishikawa, K. Shiroshita, H. Higuchi, Y. Okumura, Y. Haseba, S. I. Yamamoto, K. Sago and H. Kikuchi, *Adv. Mater.*, 2017, **29**, 1702354.
4 R. J. Mandle, S. J. Cowling and J. W. Goodby, *Phys. Chem. Chem. Phys.*, 2017, **19**, 11429–11435.
5 C. Parton-Barr, H. F. Gleeson and R. J. Mandle, *Soft Matter*, 2023, **20**, 672–680.
6 X. Chen, E. Korblova, D. Dong, X. Wei, R. Shao, L. Radzihovsky, M. A. Glaser, J. E. MacLennan, D. Bedrov, D. M. Walba and N. A. Clark, *Proc. Natl. Acad. Sci. U. S. A.*, 2020, **117**, 14021–14031.
7 R. Saha, P. Nepal, C. Feng, M. S. Hossain, M. Fukuto, R. Li, J. T. Gleeson, S. Sprunt, R. J. Twieg and A. Jákli, *Liq. Cryst.*, 2022, **49**, 1784–1796.
8 R. B. Meyer, L. Liebert, L. Strzelecki and P. Keller, *J. Phys. Lett.*, 1975, **36**, 69–71.
9 R. B. Meyer, *Mol. Cryst. Liq. Cryst.*, 1976, vol. 40, pp. 33–48.
10 S. T. Lagerwall, *Ferroelectric and antiferroelectric liquid crystals*, John Wiley & Sons, 1999.
11 A. Jákli, O. D. Lavrentovich and J. V. Selinger, *Rev. Mod. Phys.*, 2018, **90**, 045004.
12 K. Perera, R. Saha, P. Nepal, R. Dharmarathna, M. S. Hossain, M. Mostafa, A. Adaka, R. Waroquet, R. J. Twieg and A. Jákli, *Soft Matter*, 2022, **19**, 347–354.
13 N. Sebastián, L. Cmok, R. J. Mandle, M. R. De La Fuente, I. Drevenšek Olenik, M. Čopič and A. Mertelj, *Phys. Rev. Lett.*, 2020, **124**, 037801.
14 N. Sebastián, M. Čopič and A. Mertelj, *Phys. Rev. E*, 2022, **106**, 021001.
15 N. Sebastián, R. J. Mandle, A. Petelin, A. Eremin and A. Mertelj, *Liq. Cryst.*, 2021, **48**, 2055–2071.
16 R. Barboza, S. Marni, F. Ciciulla, F. Ali Mir, G. Nava, F. Caimi, A. Zaltron, N. A. Clark, T. Bellini and L. Lucchetti, *Proc. Natl. Acad. Sci. U. S. A.*, 2022, **119**, e2207858119.
17 M. T. Máthé, Á. Buka, A. Jákli and P. Salamon, *Phys. Rev. E*, 2022, **105**, L052701.
18 M. T. Máthé, B. Farkas, L. Péter, Á. Buka, A. Jákli and P. Salamon, *Sci. Rep.*, 2023, **13**, 6981.
19 M. T. Máthé, K. Perera, Á. Buka, P. Salamon and A. Jákli, *Adv. Sci.*, 2023, 202305950.
20 S. Nishimura, S. Masuyama, G. Shimizu, C. Chen, T. Ichibayashi and J. Watanabe, *Adv. Phys. Res.*, 2022, **1**, 2200017.
21 A. I. Jarosik, H. Nádasi, M. I. Schwidder, A. I. Manabe, M. I. Bremer, M. I. Klasen-Memmer and A. Eremin, *Proc. Natl. Acad. Sci. U. S. A.*, 2024, **121**, e2313629121.
22 J. Yang, Y. Zou, W. Tang, J. Li, M. Huang and S. Aya, *Nat. Commun.*, 2022, **13**, 7806.
23 H. Nishikawa, K. Sano and F. Araoka, *Nat. Commun.*, 2022, **13**, 1142.
24 H. Nishikawa, K. Sano, S. Kurihara, G. Watanabe, A. Nihonyanagi, B. Dhara and F. Araoka, *Commun. Mater.*, 2022, **3**, 89–99.
25 J. Li, H. Nishikawa, J. Kougo, J. Zhou, S. Dai, W. Tang, X. Zhao, Y. Hisai, M. Huang and S. Aya, *Sci. Adv.*, 2021, **7**, eabf5047.
26 M. T. Máthé, M. S. H. Himel, A. Adaka, J. T. Gleeson, S. Sprunt, P. Salamon and A. Jákli, *Adv. Funct. Mater.*, 2024, 2314158.
27 J. Li, R. Xia, H. Xu, J. Yang, X. Zhang, J. Kougo, H. Lei, S. Dai, H. Huang, G. Zhang, F. Cen, Y. Jiang, S. Aya and M. Huang, *J. Am. Chem. Soc.*, 2021, **143**, 17857–17861.
28 M. Lovšin, A. Petelin, B. Berteloot, N. Osterman, S. Aya, M. Huang, I. Drevenšek-Olenik, R. J. Mandle, K. Neyts, A. Mertelj and N. Sebastian, *Giant*, 2024, **19**, 100315.
29 C. L. Folcia, J. Ortega, R. Vidal, T. Sierra and J. Etxebarria, *Liq. Cryst.*, 2022, **49**, 899–906.
30 R. Xia, X. Zhao, J. Li, H. Lei, Y. Song, W. Peng, X. Zhang, S. Aya and M. Huang, *J. Mater. Chem. C*, 2023, **11**, 10905–10910.
31 V. Sultanov, A. Kavčič, E. Kokkinakis, N. Sebastián, M. V. Chekhova and M. Humar, *Nature*, 2024, **631**, 294–299.
32 F. Hassan, D. Yang, L. Saadaoui, Y. Wang, I. Drevensek-Olenik, Z. Qiu, J. Shao, Y. Zhang, S. Gao, Y. Li, X. Zhang and J. Xu, *Opt. Lett.*, 2024, **49**, 4662.
33 A. Manabe, M. Bremer and M. Kraska, *Liq. Cryst.*, 2021, **48**, 1079–1086.
34 J. Li, R. Xia, H. Xu, J. Yang, X. Zhang, J. Kougo, H. Lei, S. Dai, H. Huang, G. Zhang, F. Cen, Y. Jiang, S. Aya and M. Huang, *J. Am. Chem. Soc.*, 2021, **143**, 17857–17861.
35 S. Dai, J. Li, J. Kougo, H. Lei, S. Aya and M. Huang, *Macromolecules*, 2021, **54**, 6045–6051.
36 E. Cruickshank, R. Walker, J. M. D. Storey and C. T. Imrie, *RSC Adv.*, 2022, **12**, 29482–29490.
37 R. J. Mandle, *Liq. Cryst.*, 2022, **49**, 2019–2026.
38 P. Nepal, Design and Synthesis of Novel Organic Materials for Liquid Crystal Applications[Doctoral dissertation, Kent State University]. OhioLINK Electronic Theses and Dissertations Center, **https://rave.ohiolink.edu/etdc/view?acc_num=kent165914800069764**, 2022.
39 P. Guragain, Synthesis and properties of ferronematic and short tail columnar liquid crystals. [Doctoral dissertation, Kent State University]. OhioLINK Electronic Theses and Dissertations Center. **https://rave.ohiolink.edu/etdc/view?acc_num=kent1700489781814843**, 2023.
40 N. Tufaha, E. Cruickshank, D. Pociecha, E. Gorecka, J. M. D. Storey and C. T. Imrie, *Chem. – Eur. J.*, 2023, **29**, e202300073.
41 J. Karcz, J. Herman, N. Rychłowicz, P. Kula, E. Górecka, J. Szydlowska, P. W. Majewski and D. Pociecha, *Science*, 2024, **384**, 1096–1099.
42 Y. Song, M. Deng, Z. Wang, J. Li, H. Lei, Z. Wan, R. Xia, S. Aya and M. Huang, *J. Phys. Chem. Lett.*, 2022, **13**, 9983–9990.
43 Y. Song, J. Li, R. Xia, H. Xu, X. Zhang, H. Lei, W. Peng, S. Dai, S. Aya and M. Huang, *Phys. Chem. Chem. Phys.*, 2022, **24**, 11536–11543.

44 M. V. Reddy, B. Veeraprakash, B. M. B. Mahesh, M. Ramanjaneyulu and P. V. P. Venkateswarlu, *Orient. J. Chem.*, 2023, **39**, 144–153.
45 M. Funahashi and T. Kato, *Liq. Cryst.*, 2015, **42**, 909–917.
46 Y. Li, A. Concellón, C. J. Lin, N. A. Romero, S. Lin and T. M. Swager, *Chem. Sci.*, 2020, **11**, 4695–4701.
47 M. Funahashi and J. I. Hanna, *Adv. Mater.*, 2005, **17**, 594–598.
48 L. Wang, W. He, X. Xiao, Q. Yang, B. Li, P. Yang and H. Yang, *J. Mater. Chem.*, 2012, **22**, 2383–2386.
49 Y. Arakawa, Q. Ning, S. Karthick and S. Aya, *J. Mater. Chem. C*, 2024, **12**, 16206–16217.
50 K. Perera, R. Saha, P. Nepal, R. Dharmarathna, M. S. Hossain, M. Mostafa, A. Adaka, R. Waroquet, R. J. Twieg and A. Jákli, *Soft Matter*, 2022, **19**, 347–354.
51 P. Nacke, A. Manabe, M. Klasen-Memmer, X. Chen, V. Martinez, G. Freychet, M. Zhernenkov, J. E. Maclennan, N. A. Clark, M. Bremer and F. Giesselmann, *Sci. Rep.*, 2024, **14**, 4473.
52 X. Chen, V. Martinez, P. Nacke, E. Korblova, A. Manabe, M. Klasen-Memmer, G. Freychet, M. Zhernenkov, M. A. Glaser, L. Radzihovsky, J. E. Maclennan, D. M. Walba, M. Bremer, F. Giesselmann and N. A. Clark, *Proc. Natl. Acad. Sci. U. S. A.*, 2022, **119**, e2210062119.
53 R. J. Mandle, N. Sebastián, J. Martinez-Perdiguero and A. Mertelj, *Nat. Commun.*, 2021, **12**, 4962.
54 A. Mertelj, L. Cmok, N. Sebastián, R. J. Mandle, R. R. Parker, A. C. Whitwood, J. W. Goodby and M. Čopič, *Phys. Rev. X*, 2018, **8**, 041025.
55 A. de Vries, *Mol. Cryst. Liq. Cryst.*, 1970, **10**, 219–236.
56 H. Kikuchi, H. Matsukizono, K. Iwamatsu, S. Endo, S. Anan and Y. Okumura, *Adv. Sci.*, 2022, **9**, 2202048.
57 G. J. Strachan, E. Górecka, J. Hobbs and D. Pociecha, *J. Am. Chem. Soc.*, 2025, **147**, 6058–6066.
58 J. Hobbs, C. J. Gibb, D. Pociecha, J. Szydłowska, E. Górecka and R. J. Mandle, *Angew. Chem., Int. Ed.*, 2025, **64**, e202416545.
59 R. G. Petschek and K. M. Wiefling, *Phys. Rev. Lett.*, 1987, **59**, 343.
60 D. R. Perchak and R. G. Petschek, *Phys. Rev. A: At., Mol., Opt. Phys.*, 1991, **43**, 6756.
61 P. Palffy-Muhoray, M. A. Lee and R. G. Petschek, *Phys. Rev. Lett.*, 1988, **60**, 2303.
62 N. V. Madhusudana, *Phys. Rev. E*, 2021, **104**, 014704.
63 A. Chrzanowska and L. Longa, *arXiv*, 2024, preprint, arXiv:2409.09851v1.
64 W. H. De Jeu, W. J. A. Goossens and P. Bordewijk, *J. Chem. Phys.*, 1974, **61**, 1985–1989.

